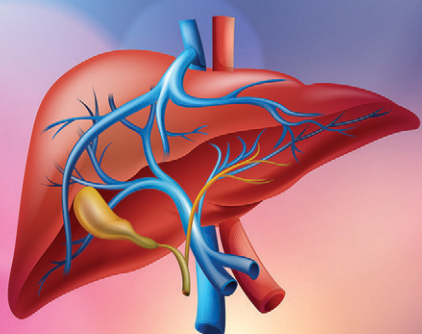


# Lab on a Chip

Devices and applications at the micro- and nanoscale

rsc.li/loc



ISSN 1473-0197



ROYAL SOCIETY  
OF CHEMISTRY

Celebrating  
IYPT 2019

## COMMUNICATION

Yu Shrike Zhang *et al.*

A miniaturized optical tomography platform for volumetric imaging of engineered living systems

Cite this: *Lab Chip*, 2019, **19**, 550Received 31st October 2018,  
Accepted 3rd January 2019

DOI: 10.1039/c8lc01190g

rsc.li/loc

## A miniaturized optical tomography platform for volumetric imaging of engineered living systems†

Adem Polat,<sup>‡abc</sup> Shabir Hassan, <sup>iD</sup><sup>‡a</sup> Isa Yildirim, <sup>bd</sup> Luis Eduardo Oliver,<sup>a</sup> Maryam Mostafaei, <sup>iD</sup><sup>ae</sup> Siddharth Kumar, <sup>af</sup> Sushila Maharjan, <sup>iD</sup><sup>ag</sup> Louis Bourguet,<sup>a</sup> Xia Cao, <sup>iD</sup><sup>ah</sup> Guoliang Ying, <sup>ai</sup> Milad Eyyazi Hesar<sup>aj</sup> and Yu Shrike Zhang <sup>iD</sup><sup>\*a</sup>

Volumetric optical microscopy approaches that enable acquisition of three-dimensional (3D) information from a biological sample are attractive for numerous non-invasive imaging applications. The unprecedented structural details that these techniques provide have helped in our understanding of different aspects of architecture of cells, tissues, and organ systems as they occur in their natural states. Nonetheless, the instrumentation for most of these techniques is sophisticated, bulky, and costly, and is less affordable to most laboratory settings. Several miniature imagers based on webcams or low-cost sensors featuring easy assembly have been reported, for *in situ* imaging of biological structures at low costs. However, they have not been able to achieve the ability of 3D imaging throughout the entire volumes for spatiotemporal analyses of the structural changes in these specimens. Here we present a miniaturized optical tomography (mini-Opto) platform for low-cost, volumetric characterization of engineered living systems through hardware optimizations as well as applications of an optimized algebraic algorithm for image reconstruction.

## Introduction

Since its invention in the 17th century, light microscopy has been at the forefront of visual diagnostics in pathology and cell biology studies to perform morphological analysis, detection, and identification.<sup>1</sup> The interaction of light with biological tissues has been used to decipher details regarding tissue morphology, disease status, and biological functions on the microscopic, mesoscopic, and macroscopic levels.<sup>2</sup> For a long time, biomedical samples of planar nature have been used after processing into thin sections, for yielding various types of two-dimensional (2D) information through conventional light microscopy.<sup>3,4</sup> However, this strategy is unsuitable for obtaining three-dimensional (3D) anatomy as the data lack information regarding the original positions within the specimens.<sup>5,6</sup> In addition, the requirement of sectioning is destructive, which does not allow for repeated measurements of the same samples over extended periods of time. The use of multiple samples may also increase the probability of errors originating from variations in the specimens. With the invention of 3D imaging modalities such as confocal, multi-photon, and light-sheet microscopy, the unprecedented volumetric details that these techniques provide have helped in our understanding of different organelles, cells, and tissues as they occur in their natural state as well as in engineered living systems.<sup>4,7–10</sup>

Among the different engineered living systems, microphysiological systems are important tools that produce a microenvironment representative of the *in vivo* conditions,<sup>11–13</sup> which are anticipated to model human tissues and organs better than conventional planar, static cell cultures, and animals in certain cases.<sup>14,15</sup> These cellular assemblies, usually in 3D formats featuring integrated dynamic cues, mimic tissue organization, and have the capability to reproduce molecular and cellular events *in vitro*. As such, they can be effectively used for more accurate drug screening and for achieving personalized medicine through utilizing patient-derived cells/tissues in building the models.<sup>16,17</sup> To

<sup>a</sup> Division of Engineering in Medicine, Department of Medicine, Brigham and Women's Hospital, Harvard Medical School, 65 Landsdowne St, Cambridge, MA 02139, USA. E-mail: yszheng@research.bwh.harvard.edu

<sup>b</sup> Istanbul Technical University, Faculty of Electrical and Electronics Engineering, Institute of Informatics, 34469, Maslak, Istanbul, Turkey

<sup>c</sup> Department of Electrical and Electronics Engineering, Adana Science and Technology University, Adana, Turkey

<sup>d</sup> College of Engineering, University of Illinois, Chicago, IL 60607, USA

<sup>e</sup> MAS Medical Physics, Department of Physics, ETH Zurich, Zurich 8093, Switzerland

<sup>f</sup> BITS Pilani, K. K. Birla Goa Campus, Goa 403726, India

<sup>g</sup> Research Institute for Bioscience and Biotechnology, Nakkhu-4, Lalitpur 44600, Nepal

<sup>h</sup> Department of Pharmaceutics and Tissue Engineering, School of Pharmacy, Jiangsu University, Zhenjiang 212013, P.R. China

<sup>i</sup> School of Materials Science and Engineering, Wuhan Institute of Technology, Wuhan 430205, P.R. China

<sup>j</sup> Institute of Materials in Electrical Engineering 1 (IWE1), RWTH Aachen University, 52062 Aachen, Germany

† Electronic supplementary information (ESI) available. See DOI: 10.1039/c8lc01190g

‡ Authors contributed equally.

understand how the cells behave and/or respond to pharmaceutical compounds, it is also strongly desirable to obtain the chronological and volumetric information within the micro-physiological systems, ideally in a non-invasive manner.<sup>18–20</sup> Hurdles including being costly and thus unaffordable have limited the aforementioned high-end 3D imaging techniques in practical use as easily as one could wish.

More recently, several miniature imagers based on webcams or portable sensors have been reported for *in situ* imaging of biological structures at unprecedentedly low costs.<sup>21–26</sup> For example, we have previously built a mini-microscope that was directly integratable with microfluidic

bioreactors for continuous monitoring of cell migration, proliferation, and fluid flow for applications in micro-physiological systems.<sup>23,27,28</sup> Due to the low costs and small form factors, these mini-microscopes can be attached in a parallel fashion to simultaneously interface with a number of bioreactors to study organoid behaviors in real-time and non-invasively. However, they have rarely been able to achieve the ability of 3D imaging throughout the entire volumes of the specimens for spatiotemporal analyses of the structural changes. Different image reconstruction algorithms have also been used to enhance the information that is obtained from various biomedical specimens in conjunction with the high-

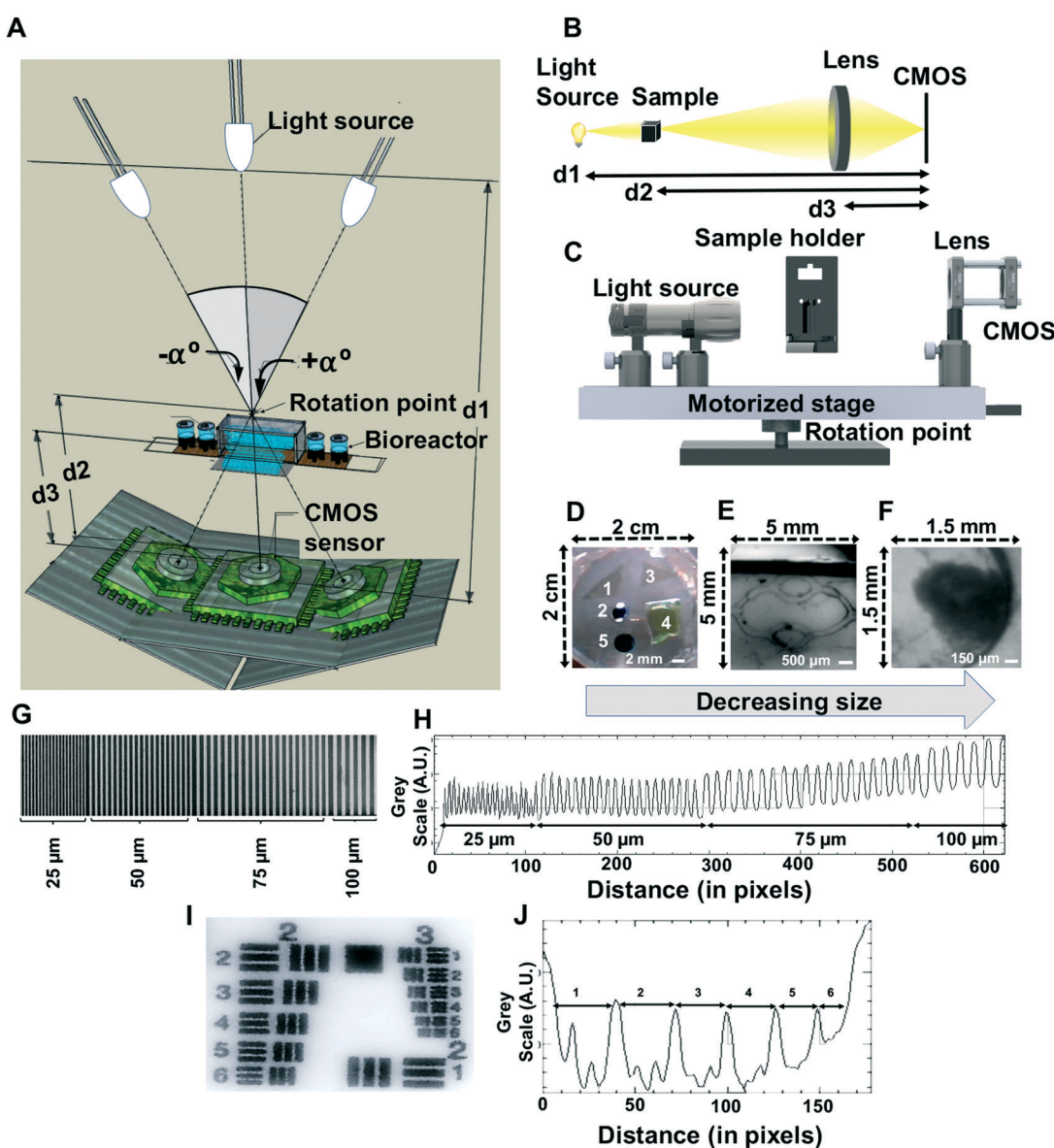


**Fig. 1** A) Geometry, B) ray diagram, and C) optomechanical components of the mini-Opto setup.  $d_1$ ,  $d_2$ , and  $d_3$  are the distances between the light source and the CMOS, sample and the CMOS, lens, and the CMOS, respectively. D–F) Different specimens used for characterizing the mini-Opto: D) objects in a PDMS matrix, E) sacrificially bioprinted vascular channels in a hydrogel, and F) tumoroid of MCF-7 breast cancer cells in a bioreactor, showing different samples varying in size that can be imaged by the setup. G and I) Different resolution test patterns used to obtain the one-dimensional (1D) profiles in H) the vertical lines and J) horizontal lines of element 6, group 3 of USAF 1951, respectively, of the resolution test patterns using the mini-Opto setup.

end optical methods,<sup>29–32</sup> but almost none have been developed for miniature, low-cost, non-invasive microscopy.

Here, we present a miniaturized optical tomography (mini-Opto) platform for low-cost volumetric characterization of microphysiological systems through both hardware optimizations and an optimized algebraic algorithm for image reconstruction and analysis. We show the feasibility of this imaging technology in assessing engineered tissue models. Widespread utility of this non-invasive, non-expensive, easy-to-use optical setup, that can be integrated with microfluidic bioreactors or different engineered living systems of interest for continual monitoring of morphological and possibly biophysicochemical features in 3D at reasonable resolution, is anticipated.

## Materials and methods

### Optical assembly setup

The optical design of the tool was inspired from X-ray computed tomography. The geometry, ray diagram, and main components of the mini-Opto platform are illustrated in Fig. 1A–C and S1.† It consisted of a light source for illumination, a plano-convex lens to focus the non-coherent beam from the light source, and a complementary metal-oxide-semiconductor (CMOS; OmniVision Technologies Inc.) sensor for image formation. A light-emitting diode (LED; 60 mW; DiCUNO) of broad-spectrum shining light in the visible region was used as the light source. An achromatic anti-reflective visible-infrared coated lens with a 10-mm diameter and a 30-mm focal length (Edmund Optics) was used to focus the transmitted light onto the CMOS sensor.

### Mechanical setup

The mechanical setup of the mini-Opto is illustrated in Fig. S1.† For the rotating axis to be able to carry the load of all the optical components and the sample, the main body-frame of the platform was built from 20-mm T-slotted black anodized aluminum. The scans were taken by keeping the sample on the holder and starting with 0° scan and moving the stage at 5° per step with the assistance of two stepper motors (Sparkfun Electronics) between +45° and -45°. To decrease the noise from vibration while scanning, the sample holder was decoupled from the motorized rotating arm of the scanning stage of the mini-Opto. The sample holder was adjusted on the external support of the platform. Two motorized rails were used to control the linear freedom of the sample holder for the forward (towards) and backward (away) motion with respect to the CMOS sensor. Additionally, an extra micro-stepping linear stepper motor (Karlsson Robotics) was used to provide the freedom of moving the sample in the +z and -z (vertical) directions. All the stepper motors were programmed to have an electronic control for precise movements. The scans were saved after being recorded by the CMOS sensor and reconstructed using a custom-developed MATLAB-based software package.

### Software for mini-Opto

Our recently developed compressed sensing (CS)-based iterative reconstruction method, which we term as ART+TV<sub>3D</sub> (3D total variation (TV)-regularized algebraic reconstruction technique (ART)),<sup>33</sup> was adapted to create the software designed specifically for the mini-Opto using MATLAB (Mathworks). In addition to the 3D image reconstruction of the sample, the software also dealt with the challenges associated with limited view angle image reconstruction by ART, such as image blur, among others. To execute the software, a MATLAB-based user interface was further developed. The flowchart of the algorithm is shown in Fig. S2.†

### Phantom preparation

To validate the imaging ability and penetration depth for 3D volume information of the mini-Opto platform for imaging different microphysiological systems, a series of relevant samples were prepared for analysis. In particular, three phantoms/specimens were chosen (Fig. 1D–F).

The first phantom had different artificial objects separated in space in a polydimethylsiloxane (PDMS) matrix. For this phantom, differently shaped objects of varied sizes at different heights were placed inside a solid PDMS matrix with a dimension of 2.8 cm × 2 cm × 2 cm (Fig. 1D).

A sacrificial-bioprinted vascular channel was incorporated in gelatin methacryloyl (GelMA) to prepare the second specimen. GelMA was synthesized as we previously reported.<sup>34</sup> Briefly, 10% w/v of powdered gelatin type A from porcine skin (Sigma-Aldrich) was dissolved in Dulbecco's phosphate-buffered saline (DPBS; Thermo Fisher) and stirred at 60 °C until its complete dissolution. To the mixture, 8% (v/v) of methacrylic anhydride (Sigma-Aldrich) was gradually added while constantly stirring the mixture, representing a high methacryloyl substitution degree of ~80%.<sup>35</sup> The reaction was carried out at constant stirring for 1 h at 60 °C and 500 rpm. Two volumes of pre-heated (60 °C) DPBS was added to the solution. This was followed by dialysis of the solution mixture using a 12–14 kDa cutoff dialysis membrane (Thermo Fisher) against deionized water. Dialysis was carried out for 1 week, after which the solution was filtered, and placed at -80 °C to freeze before lyophilizing. At the end of lyophilization, freeze-dried GelMA was obtained in the form of a white porous foam and was mixed with DPBS containing 0.5% (w/v) 2-hydroxy-1-(4-(hydroxyethoxy)-phenyl)-2-methyl-1-propanone (Irgacure 2959, Sigma-Aldrich) as the photoinitiator. The microfluidic channel was prepared from sacrificial bioprinting.<sup>34</sup> Using a bioprinter (Allevi 1) equipped with a 26G blunt needle, a 3D sacrificial microfibrous template made of 40% (w/v) Pluronic F-127 (Sigma-Aldrich) in water was deposited to mimic the branching vasculature. Following overnight dehydration, the printout was placed at an inclination (45°) inside a PDMS mold of 8 mm (length) × 4 mm (width) × 4 mm (depth) in size, filled with GelMA prepolymer at 10% (w/v), and cured under UV (Omnicure, power: 850 mW cm<sup>-2</sup>) for 30–45 s. The inclination was done in a way to not have the channel in a horizontal plane but traverse the volume of the hydrogel so that different

features would focus in different layers and hence test the mini-Opto for volumetric information after image reconstruction. After crosslinking, the block was placed in cold DPBS at 4 °C for 15 min. The liquefied sacrificial microfiber of Pluronic was then removed using mild suction with a syringe needle to generate the vascular channels (Fig. 1E).

For the third specimen, tumor spheroids were produced following established protocols using microwells<sup>36–39</sup> and a breast cancer cell line, MCF-7 (Fig. 1F). PDMS microwells (200 µm in diameter) were created using standard lithography technique for spheroid generation. Upon collection, the spheroids were then resuspended in GelMA (80% methacryloyl substitution) prepolymer solution at 6% (w/v), and molded into a previously described bioreactor with a chamber size of 7 cm × 7 cm × 1 cm.<sup>40–43</sup> UV illumination at 800 mW m<sup>-2</sup> for 30 s was used to crosslink the GelMA matrix.<sup>28,34,41,43–46</sup> The breast tumor spheroid-encapsulating bioreactor was placed in culture and monitored for up to 6 days and imaged every 2 days after retrieving from the incubator and placed on the sample stage of the mini-Opto for volumetric imaging analysis.

## Results and discussion

### Algorithmic image processing through iterative ART+TV<sub>3D</sub>

The iteration was initiated by creating an initial estimate of the object to be imaged and its forward projection was computed. The difference between the forward projected data and the measured (detector) data was calculated as the error. This error or correction term was back-projected to minimize the error through averaging. The process was repeated for a number of iterations until the error was small enough to be ignored.<sup>47</sup> ART was used in problems involving different geometries and limited projection angles.<sup>48</sup> Historically, the technique was introduced by Kaczmarz initially for solving linear systems of equations,<sup>47,49</sup> which was then used in different medical imaging applications.<sup>50</sup> Fig. S2A† depicts the different steps that are involved in an iterative reconstruction algorithm.

The reconstruction process starts with solving a linear algebraic equation:

$$A \cdot \vec{X} = \vec{Y}, \quad (1)$$

where  $\vec{X}$  is a column vector that contains the values of all the pixels in the image,  $\vec{Y}$  is a column vector where one finds the results of all the projections for every ray of every angle, and  $A$  is the system matrix that includes the weight of each voxel for different rays passing through the object and hitting the detector pixels and thus represents a weight matrix. This weight matrix contains the weight of every pixel for all the different rays in the projection. These weights are the important indicators for a pixel value in a particular ray and thus are very important components of the ART reconstruction process. The ART is based on a simple principle that every pixel density is spread over the reconstruction space where they are modified after each iteration. This allows the

reconstructed projection to approach the measured projection. Basically, ART changes the grayness of pixels on the intersections of the rays to make the ray sum correspond to the measured projection. Mathematically, eqn (1) can be written in an expanded form as a system of linear equations, which should be solved when reconstructing an image:

$$\begin{aligned} a_{11}x_1 + a_{12}x_2 + a_{13}x_3 + \dots + a_{1m}x_m &= y_1 \\ a_{21}x_1 + a_{22}x_2 + a_{23}x_3 + \dots + a_{2m}x_m &= y_2 \\ a_{31}x_1 + a_{32}x_2 + a_{33}x_3 + \dots + a_{3m}x_m &= y_3 \\ \dots \\ a_{n1}x_1 + a_{n2}x_2 + a_{n3}x_3 + \dots + a_{nm}x_m &= y_n, \end{aligned} \quad (2)$$

where  $m$  represents the number of voxels of the object,  $n$  represents the number of the incident ray components within each projection, and  $a_{ij}$  represents weight coefficients of the system matrix  $A$ .<sup>51</sup> Applying the incident ray components for  $i = 1, 2, 3, \dots, N$  and voxel components for  $j = 1, 2, 3, \dots, M$ , where  $N$  and  $M$  are respectively the ray number and voxel number, the image output,  $X_j^{(k+1)}$ , using ART is given by:

$$X_j^{(k+1)} = X_j^{(k)} + \frac{Y_i \sum_{m=1}^M a_{im} X_m^{(k)}}{\sum_{m=1}^M a_{im}^2} a_{ij}, \quad (3)$$

where  $X_j^{(k)}$  is the current image,  $Y_i$  is the measured projection data corresponding to the  $i^{\text{th}}$  ray line integral,  $\sum_{m=1}^M a_{im}^2$  is the normalization factor,  $a_{ij}$  represents weight coefficients of the matrix,  $m$  represents the number of voxels of the object, and  $n$  represents the number of rays within each projection (Fig. S2B†). The contribution of  $j^{\text{th}}$  voxel on the  $i^{\text{th}}$  ray line integral is weighted by the system coefficient  $a_{ij}$ .  $a_{ij}$  is also termed as the Siddon's coefficients.<sup>52</sup> A single iteration means that the updating was repeated for all the projections hitting the image at a particular region from different angles. The reconstruction algorithm was finished when a convergence criterion was satisfied. Fig. S2C† shows the flowchart of the ART algorithm.

Applying ART as such for iterative and reconstruction purposes is inherently very noisy. The noise is elevated with an increase in the number of scans. As such, CS was used to reconstruct images from minimal number of scans of our sample. The CS technique is based on the principle that, through optimization, the sparsity of a signal can be exploited to recover it from far fewer samples than required by a previous theorem, the Shannon-Nyquist sampling theorem (NYQ). The NYQ sampling theory builds on the assumption that sampling frequency of a signal ( $f_{\text{NYQ}}$ ) must be at least two times faster than its bandwidth ( $W$ ) for a lossless uniform sampling, *i.e.*, ( $f_{\text{NYQ}} \geq 2W$ ). Since images are not bandlimited, the sampling rate is specified by the desired spatial resolution and not by the Shannon theorem. In case the number of sampling is much less than the Nyquist rate ( $f_{\text{cs}} \ll f_{\text{NYQ}}$ ), the CS method is used instead. CS relies on two

conditions: sparsity and incoherence. Sparsity requires the signal to be sparse in some domain. The object being recovered must be sparse or at least can be sparsified.<sup>53</sup> Incoherence is applied through the isometric property, which is sufficient for sparse signals. For the imaging model described in this paper, the CS-based reconstruction algorithm was formulated as a constraint minimization problem and is described as follows:

$$\hat{X} = \underset{x}{\arg \min} \|\varphi X\|_{l=0} \quad \text{such that } Y = AX, \quad (4)$$

where  $\varphi$  is termed sparsifying operator and sparsifies  $X$ . Sparsifying transformation was used because natural images are not sparse in general but can be sparsified easily by exploiting their uniformity. The TV operator was used as the sparsifying operator. Rudin, Osher, and Fatemi (ROF) introduced the TF method as a regularizing criterion for solving inverse problems in 1992.<sup>54</sup> Since then, ROF has evolved over time and can be used in regularizing images without smoothing the boundaries of the objects.<sup>54</sup>  $l_2$ -Norm TV can be described as:

$$\|\text{TV}(X)\|_2 = \sum_{i=1}^N \|D_i X\|_2, \quad (5)$$

where  $D_i$  is the forward difference approximation to the gradient at voxel  $i$ . Expanded form of TV in 3D can be written as:

$$\text{TV}_{3D}(X) = \sum_k^K \sum_j^J \sum_i^I \sqrt{(X_{i,j,k} - X_{i-1,j,k})^2 + (X_{i,j,k} - X_{i,j-1,k})^2 + (X_{i,j,k} - X_{i,j,k-1})^2}, \quad (6)$$

where  $X_{i,j,k}$  represents the intensity value at voxel  $(i,j,k)$ ,  $i = 1, 2, \dots, I$ ;  $j = 1, 2, \dots, J$ ;  $k = 1, 2, \dots, K$ . The dimensions of the 3D object in the directions of  $X$ ,  $Y$ ,  $Z$  are given by  $I$ ,  $J$ ,  $K$ , respectively. CS-based iterative reconstruction, named as ART+TV<sub>3D</sub>, used in our reconstructions was obtained by solving the following unconstrained minimization formula:

$$\hat{X} = \underset{x}{\arg \min} \left[ \|Y^{\text{meas}} - Y^{\text{cal}}\|_2^2 + \lambda \|\text{TV}(X)\|_2 \right], \quad (7)$$

where  $\lambda$  is the regularization coefficient controlling the effect of the TV on the final output. This minimization problem was performed by using the gradient descent algorithm. The gradient of the  $l_2$ -norm of 3D TV is given by:

$$\begin{aligned} \text{Grad}(X) = \frac{d\text{TV}[X]}{dX_{(i,j,k)}} &= \frac{3X_{(i,j,k)} - X_{(i+1,j,k)} - X_{(i,j+1,k)} - X_{(i,j,k+1)}}{\sqrt{(X_{(i,j,k)} - X_{(i+1,j,k)})^2 + (X_{(i,j,k)} - X_{(i,j+1,k)})^2 + (X_{(i,j,k)} - X_{(i,j,k+1)})^2 + \varepsilon}} \\ &+ \frac{X_{(i,j,k)} - X_{(i-1,j,k)}}{\sqrt{(X_{(i-1,j,k)} - X_{(i,j,k)})^2 + (X_{(i-1,j,k)} - X_{(i-1,j+1,k)})^2 + (X_{(i-1,j,k)} - X_{(i-1,j,k+1)})^2 + \varepsilon}} \\ &+ \frac{X_{(i,j,k)} - X_{(i,j-1,k)}}{\sqrt{(X_{(i,j-1,k)} - X_{(i+1,j-1,k)})^2 + (X_{(i,j-1,k)} - X_{(i,j,k)})^2 + (X_{(i,j-1,k)} - X_{(i,j-1,k+1)})^2 + \varepsilon}} \\ &+ \frac{X_{(i,j,k)} - X_{(i,j,k-1)}}{\sqrt{(X_{(i,j,k-1)} - X_{(i+1,j,k-1)})^2 + (X_{(i,j,k-1)} - X_{(i,j+1,k-1)})^2 + (X_{(i,j,k-1)} - X_{(i,j,k)})^2 + \varepsilon}} \end{aligned} \quad (8)$$

The value of the term  $\varepsilon$  was chosen such that there was a non-zero term in the denominator. The regularization coefficient ( $\lambda$ ) of ART+TV<sub>3D</sub> was chosen at a fixed value of 5, empirically.

## Characterizations of the mini-Opto

The resolution of our mini-Opto imaging platform was illustrated using two different photographic resolution targets, to resolve the vertical lines shown in four groups of 100–25  $\mu\text{m}$  interspaces (Fig. 1G) or the grouped patterns from a USAF 1951 test target (Fig. 1I). From the results in Fig. 1H, the mini-Opto imaging system was able to resolve the closest target lines in the 25  $\mu\text{m}$  interspaced group individually from Fig. 1G, indicating that the resolution was better than 25  $\mu\text{m}$ . For the target pattern in Fig. 1I where the least separation between two lines of element 6 in group 3 was 35.08  $\mu\text{m}$ , the mini-Opto could resolve the lines with clear peak separation (Fig. 1J). The results from these two test targets indicated that the imaging system could resolve structures down to 25  $\mu\text{m}$  in size with good precision under the current optical setup. However, it is important to note that this resolution does not necessarily translate to the resolution one would retrieve from imaging 3D microphysiological systems. The resolution targets were in 2D embedded in air as a medium for the transmitted light to be detected by the CMOS sensor. For

an engineered 3D system, however, one has to take into account the amount of information that is lost due to the scattering/absorption events of the medium that hosts cellular or tissue structures and as such the reduced resolution in a sample-dependent manner.<sup>55</sup>

These effects also influence the depth information that can be obtained from the imaging system. To obtain the 3D volume information of any specimen, it is important to have the maximum depth information possible. To evaluate the 3D imaging capability of the mini-Opto imaging tool, five objects of varied shapes and sizes were placed at different depths inside a cylindrical PDMS matrix of 2 cm in diameter and 2 cm in thickness (Fig. 2A–C). The sample was placed on the sample holder of the imaging tool. Although the system was able to take a total of 19 projections, for our reconstruction

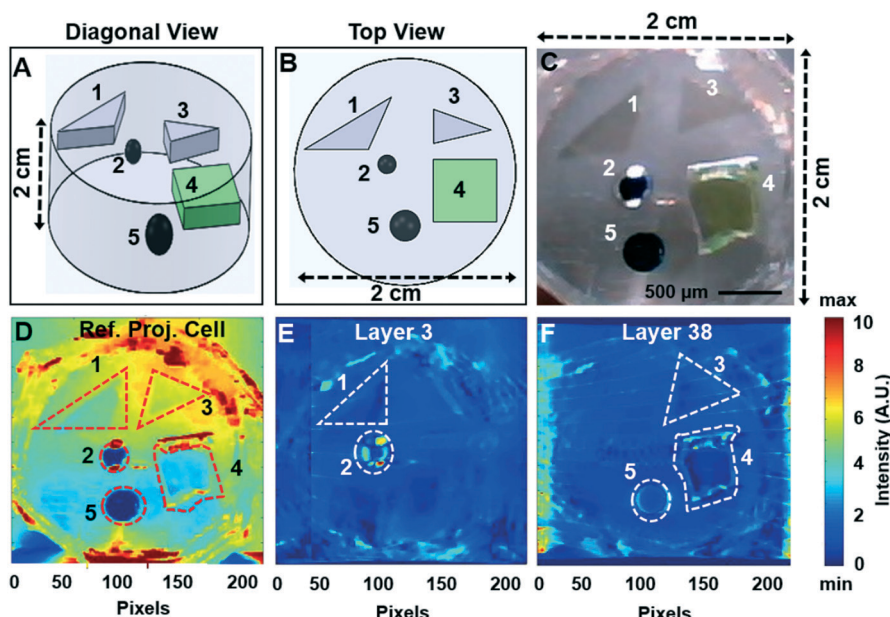


**Fig. 2** PDMS phantom, reference projection, and reconstructed images. A and B) Schematic of the phantom showing the diagonal and top views of phantom. C) Photo of the actual phantom, which included five elements, numbered 1–5, respectively. D) Reference projection of the phantom with a dimension of  $200 \times 200$  pixels in MATLAB. Resolution was  $100 \mu\text{m}$  per pixel. E and F) The 3rd and 38th layers in the reconstruction of the phantom showing the evolution of the structural features of different objects separated in space in the PDMS matrix.

we found that only 11 projections were sufficient. Starting at  $0^\circ$  (in plane with the light source and the CMOS sensor) and scanning at  $5^\circ$  per step to the right (+) and left (-) of this plane until  $25^\circ$  on each side were obtained and the images were used for further analysis. The dimension of each projection was  $200 \times 200$  pixels. Depending upon the sample dimensions and the resolution needed, one could take less or more number of projections as well to achieve optimal imaging. For the processing, the image voxels were updated ray by ray for each projection. This process was repeated for all projections to complete a single iteration using the ART. The iteration was further processed with the ART+TV<sub>3D</sub> method using eqn (6). As mentioned earlier, a preset value of 5 for the TV regularization coefficient ( $\lambda$ ) was used for all reconstructions. Although it is well-known that  $\lambda$  should be selected inversely proportional to signal-to-noise ratio (SNR),<sup>56,57</sup> there exists no gold standard for choosing it. As described in the flowchart in Fig. S2C,<sup>†</sup> the MATLAB code followed three main steps: the first step calculated the intersection lengths and their indices, the second step built the system matrix, and the third step performed ART and ART+TV<sub>3D</sub> operations.

The reference projection taken at  $0^\circ$  was used to evaluate the relevance of image acquisition setup, and is illustrated in Fig. 2D, while Fig. 2E and F show the reconstructed 3D volume data formed from the 11 scanned projections of the phantom taken at the different angles, at layer 3 and layer 38 from the reconstructed volumetric data. As clearly indicated, the different objects evolved in the different layers. In the 3rd layer, the structural features of the objects 1 and 2 in focus could be observed in close proximity to each other in the PDMS matrix. Similarly, objects 3, 4, and 5 were also placed

in close proximity to each other but further in depth from objects 1 and 2 in the PDMS matrix. This difference in their positions in the matrix made them appear in different layers in the 3D rendition of the projections, where the heatmap represents the intensity of the signal. Movie S1<sup>†</sup> shows the continuous optical slices through 3D rendition where the different objects could be observed to appear or disappear based on their relative spatial arrangement in the PDMS phantom. The characterization provided proof-of-concept and feasibility of our mini-Opto platform in volumetric imaging of specimens.

#### Validation of the mini-Opto platform in analyzing micro-physiological systems

Next, the mini-Opto platform was evaluated for its utility in volumetric imaging of two categories of microphysiological systems. These included a bioprinted vascularized tissue model and a multicellular tumor spheroid model.

Ways to integrate a vascular network into the engineered tissue models are of strong demand since vascularization presents one of the greatest challenges in generating functional tissues.<sup>58–61</sup> During the past few years, bioprinting has emerged as a class of enabling technologies towards the solution of such a challenge, due to their unparalleled versatility of depositing complex tissue patterns at high fidelity and reproducibility in an automated manner.<sup>62–64</sup> A sacrificial bioprinting strategy<sup>34,65–68</sup> was used to generate our vascularized tissue construct at an inclined angle of the channel, to determine the capacity of mini-Opto in characterizing complex engineered living systems. While different microfluidic scanning-based microscopic techniques have been developed

for 3D imaging, such as optofluidic microscopy,<sup>69,70</sup> the primary downside of such techniques is that one needs high number of scans (on the order of 50–60) and high-end optical components, making them less feasible and cost-prohibitive. On the contrary, similar to the PDMS phantom, only 11 projections were needed for our mini-Opto to reconstruct the 3D volume data based on our algorithm.

As shown in Fig. 3, different features of the vascularized channel appeared in different layers. With a channel diameter of approximately 150  $\mu\text{m}$ , the vascularized construct in Fig. 3A was imaged. Fig. 3B illustrates the reference projection cell of the sample. It was interesting to note that the 150- $\mu\text{m}$  diameter of the channel in the vascularized construct could be clearly observed to evolve in different reconstruction layers as shown in Fig. 3C. Layer 30 indicated when the right end of the channel started to come in focus. As the scanning continued, this was followed by layer 40 that had both the side channels almost in the same focus. Further down the depth at layer 50, the channel features of the left side come in focus, thus scanning the channel for all its features through the entire hydrogel thickness. Fig. 3D shows the 3D volume rendering from different perspectives. Movie S2† shows stacked continuous optical slices of the entire volume where different features of the bioprinted channel could be

observed to appear or disappear based on their relative spatial arrangement in the hydrogel matrix.

Multicellular spheroids, formed by aggregation of cells compacted together by self-secreted extracellular matrix, have been long-used as enabling 3D cell culture models.<sup>71–74</sup> The use of the spheroids instead of dispersed cells might improve cellular functionality and our understanding of their responses to drug toxicity.<sup>39,42,75</sup> Moreover, the encapsulation of spheroids within suitable hydrogel matrices further allows their behaviors to mimic those observed *in vivo*. In the form of tumor spheroids, they have served as models to study efficacy and discovery of anticancer drugs for many cancer types such as colon, pancreatic, and prostate cancers.<sup>76–78</sup> Recently, they have also been used to investigate metastatic behavior of different types of liver cancers, where they were shown to develop different morphological features.<sup>79</sup>

As such, it is important to devise enabling optical platforms to study these spheroids and their morphological evolutions in the volumetric space. Digital in-line holography have been developed to study spherical microscopic objects, such as pollens, microbes, and spheroids in detail.<sup>80,81</sup> Despite their simplicity and cost-effectiveness, these systems suffer from several limitations. First, the image recovery process relies on the imposed object support of the sample that works well only when the samples are spatially sparse.<sup>82</sup> As such, many samples (*e.g.*, those with different features to be studied) will not return good results. The second issue stems from the stagnation problem that does not guarantee full image recovery during the iterative phase process.<sup>83,84</sup> While some advancements have been made to address these issues in the form of developing digital holographic microscopy fitted with optofluidic system,<sup>85</sup> the platform is not cost-effective and cannot be adopted at a mass scale. As such, it would be attractive to use our developed mini-Opto platform to probe the different morphological features of such tumoroids during their progression, which could potentially facilitate various research related with the use of these models.

To this end, a multicellular tumor spheroid was encapsulated in a GelMA hydrogel matrix to study its growth for investigating the 3D imaging capacity of the mini-Opto. The tumor spheroid of breast cancer cells, MCF-7, was formed through established protocols using microwells.<sup>36–39</sup> The breast tumor spheroid-encapsulating bioreactors was retrieved from the incubator and fitted on the holder of the mini-Opto for volumetric imaging every 2 days for up to 1 week. The design of the bioreactor followed our previous works.<sup>28,43,86</sup> Fig. 4 shows tumoroid analyses for 3 different time points at 2, 4, and 6 days, respectively, post-encapsulation. The CMOS images of the reference projections at 0° angle for 2nd, 4th, and 6th days are revealed in Fig. 4A, F, and K, respectively. Fig. 4B and C, G and H, and L and M show the zoomed-in areas of the reference projections in unprocessed forms and after MATLAB processing for the respective days of the experiment. Slices from construction layers 1, 10, and 40 to reveal the evolution of different structural features over

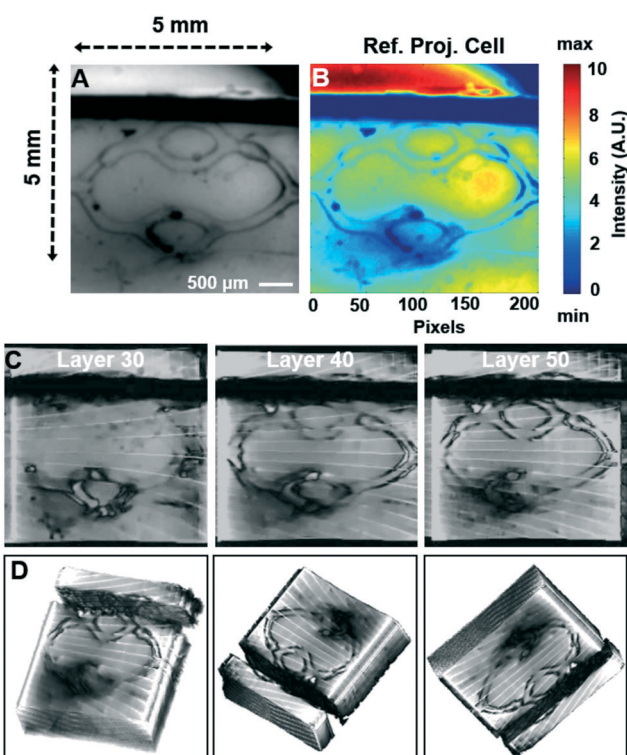


**Fig. 3** A) Top view of the phantom of a vascularized channel. B) Its reference projection with a dimension of  $200 \times 200$  pixels in MATLAB at a resolution of  $100 \mu\text{m}$  per pixel. C) The 30th, 40th, and 50th layers in the reconstruction of the phantom showing the evolution of the structural features of the vascularized channel inside a hydrogel. D) 3D volume views of the reconstruction obtained from the 50 layers, at different perspective angles.

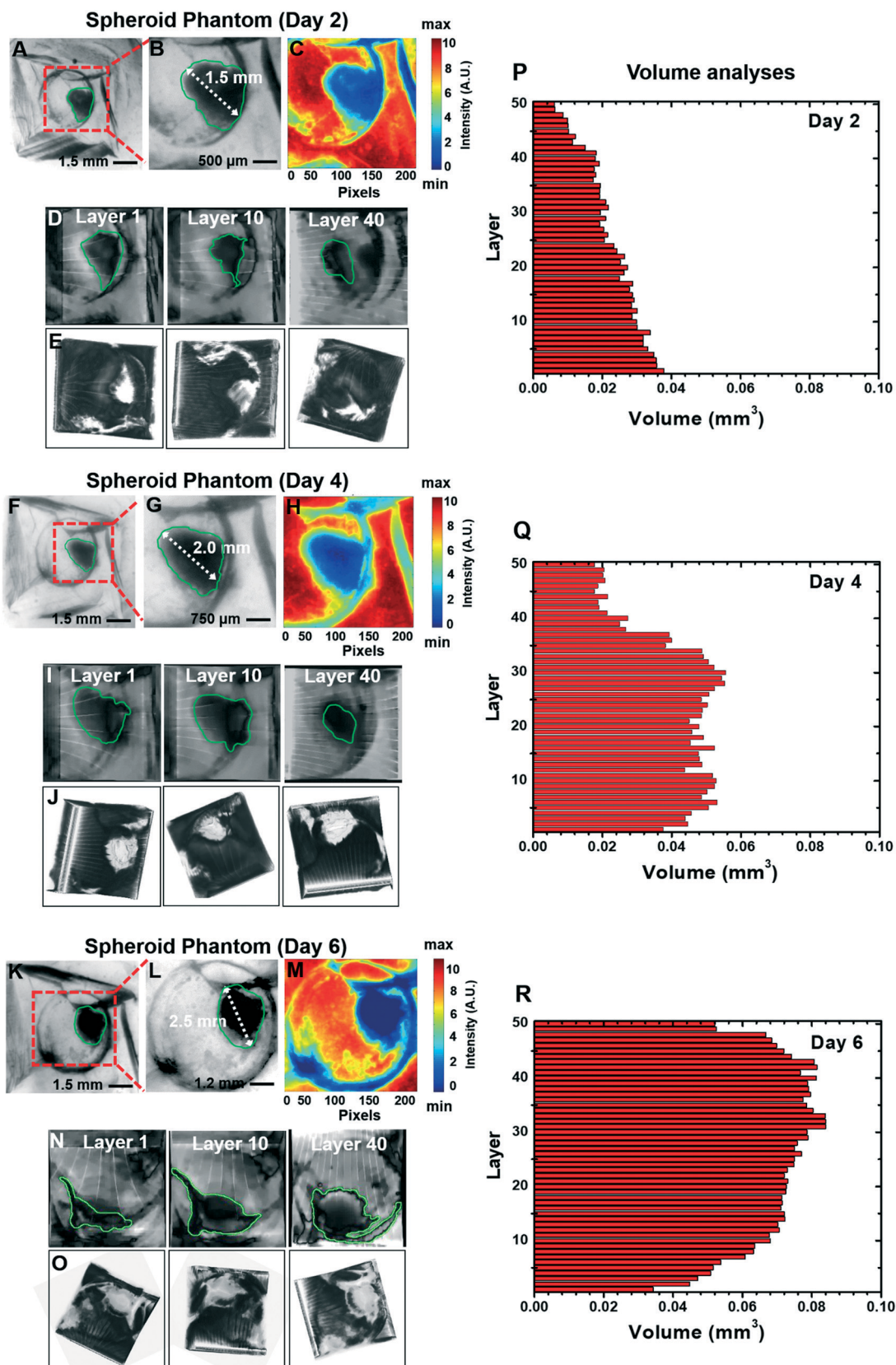


**Fig. 4** A–E), F–J), and (K–O) Tumor spheroid analyses by the mini-Opto for days 2, 4, and 6, respectively. A and B), F and G), and K and J) The images of the sample. C, H, and M) Reference projections for these samples processed in MATLAB. D, L and N) Different layers of the reconstructed images showing different structural features emerging as a function of volume (spheroid boundaries are marked with green lines). E, J, and O) 3D volume views obtained from the 50 reconstruction layers, at different perspectives (note that spheroids are shown in white against a dark background in these images to aid visualization). P, Q, and R) Individual layer volume analyses for all the 50 layers for days 2, 4, and 6, respectively.

Published on 18 January 2019. Downloaded by Singapore University of Technology and Design on 7/7/2023 5:05:56 PM.

time are shown in Fig. 4D, I, and N. The 3D volume data from different angles are shown in Fig. 4E, J, and O. The analyses indicated the morphological evolution of the spheroid over time in terms of its volume change. The morphological alterations of the tumor spheroid on 2nd, 4th, and 6th days were investigated layer by layer and calculated for the changes in volume. The projection data for individual layers are shown for day 2 in Fig. S3,<sup>†</sup> for day 4 in Fig. S4,<sup>†</sup> and for day 6 in Fig. S5,<sup>†</sup> respectively. The volumes of the 50 layers of the tumor spheroid were calculated at an axial resolution of 25 µm (*i.e.*, the optical section thickness). The respective volume changes in the tumoroid over time are plotted in Fig. 4P, Q, and R, respectively, for days 2, 4, and 6. As can be seen, there was a considerable evolution in the overall size of the tumoroid with a highest layer volume spreading from approximately 0.04 mm<sup>3</sup> on day 2 to roughly 0.09 mm<sup>3</sup> on day 6. Detailed temporal volume change comparisons from Fig. S3–S5<sup>†</sup> showed that the tumor spheroid had grown in volume from approximately 1.10 mm<sup>3</sup> on day 2 to 3.5 mm<sup>3</sup> on day 6. Such information was not possible to achieve using our previously reported mini-microscope relying on projection imaging.<sup>23</sup>

## Conclusions

We have reported the development of a miniaturized optical tomography setup for 3D volumetric characterization of microfluidic and engineered living systems. Compared to the different technologies for 3D volume data analyses, such as microfluidic-based scanning and holographic technologies, the mini-Opto platform developed in this study is cost-effective and provides a resolution that is enough to study different microfluidic and spheroid specimens. We showed 3D volumetric reconstruction of a PDMS matrix sample consisting of different objects separated along the 3D space. For microphysiological systems consisting of bioprinted microchannels representative of vasculature, we were able to reconstruct a 3D map and resolve the channels approximately 100 µm in diameter. The volumetric image reconstruction further provided us with a good growth estimate of a tumoroid embedded in a hydrogel matrix that we could follow for an extended period in a non-invasive manner successfully using our mini-Opto.

Although in the present work the samples were retrieved from the incubator for imaging outside, due to the small form factor of the mini-Opto platform, it can also be fitted into the incubator for continuous monitoring without disturbing the cultures. Working on the opto-mechanical aspects, the size of the mini-Opto can be brought down even further that will give more freedom to its use in confined incubator spaces. It is anticipated that the technology developed here can be used further to investigate differential behaviors of engineered living systems, or microphysiological systems, to study their morphological changes in response to drug treatments. While the current mini-Opto platform has been built with components costing less than \$200, one

downside of using less expensive components, *e.g.* sensors, is limited resolution. As such, the platform in its present form cannot be used to study single-cell features. Higher-end CMOS sensors<sup>87–89</sup> can be possibly adopted to improve the resolution to study single-cell level processes in the future variations of the mini-Opto, for visualizing sprouting vessels, cell migration, and tumor cell progression, among others, at slightly expanded cost. Also, automating the system with improved motors will decrease the time of image acquisition. The gained time may be used to increase the number of scans obtained from additional angles or to increase the number of scans used for image reconstructions, thereby improving the reconstruction quality of the mini-Opto. In addition, the inclusion of higher-intensity LEDs and more sensitive CMOS sensors would elevate the depth-resolving capacity of the mini-Opto especially when imaging internal structures of translucent specimens, again at the expense of elevated costs. It is also anticipated that such an improvement of optics and the relevant modification of the algorithm can equip the mini-Opto with color detection and can be used for fluorescence imaging. In addition, algorithms can be iteratively optimized to achieve automated dissection, identification, and tracking of the fine cellular features in the 3D volume, which will be reported in our future publications.

## Author contributions

A. P. and Y. S. Z. conceived the original concept. A. P., S. H., and Y. S. Z. designed the experiments and wrote the manuscript. A. P., S. H., L. E. O., M. M., S. K., S. M., L. B., X. C., G. Y., and M. E. performed the experiments and analyzed the data; I. Y. provided technical guidance on algorithms and revised the manuscript; Y. S. Z. supervised the project.

## Conflicts of interest

Authors declare no conflict of interest.

## Acknowledgements

This work was supported by the National Institutes of Health (K99CA201603, R21EB025270, R21EB026175) and the New England Anti-Vivisection Society (NEAVS). A. P. was supported by TUBITAK, the Scientific and Research Council of Turkey, under the grant 1059B141600590. S. H. acknowledges the financial support from the Swiss National Science Foundation (SNSF) under grant No. P2ZHP3\_161965 and P300PA\_177867. X. C. was supported by the National Natural Science Foundation of China (81503025). S. M. acknowledges NEAVS and the American Fund for Alternatives to Animal Research (AFAAR) for Postdoctoral Fellowship. G. L. Y. acknowledges Natural and Science Foundation of Hubei Province, China (2014CFB778).

## References

- 1 A. J. Wollman, R. Nudd, E. G. Hedlund and M. C. Leake, *Open Biol.*, 2015, 5, 150019.

- 2 G. Keiser, in *Biophotonics: Concepts to Applications*, Springer Singapore, Singapore, 2016, DOI: 10.1007/978-981-10-0945-7\_6, pp. 147–196.
- 3 R. J. Detwiler, L. J. Powers, U. H. Jakobsen, W. U. Ahmed, K. L. Scrivener and K. O. Kjellsen, *Concr. Int.*, 2001, 23, 50–58.
- 4 K. Carlsson, P.-E. Danielsson, A. Liljeborg, L. Majlöf, R. Lenz and N. Åslund, *Opt. Lett.*, 1985, 10, 53–55.
- 5 A. A. Appel, M. A. Anastasio, J. C. Larson and E. M. Brey, *Biomaterials*, 2013, 34, 6615–6630.
- 6 Y. Song, *et al.*, *J. Pathol. Inform.*, 2013, 4(Suppl S7), DOI: 10.4103/2153-3539.109864.
- 7 W. T. Mason, *Fluorescent and luminescent probes for biological activity: a practical guide to technology for quantitative real-time analysis*, Academic Press, 1999.
- 8 P. J. Verveer, J. Swoger, F. Pampaloni, K. Greger, M. Marcello and E. H. Stelzer, *Nat. Methods*, 2007, 4, 311–313.
- 9 J.-X. Cheng and X. S. Xie, *J. Phys. Chem. B*, 2004, 108(3), 827–840.
- 10 R. H. Webb, *Rep. Prog. Phys.*, 1996, 59, 427.
- 11 S. N. Bhatia and D. E. Ingber, *Nat. Biotechnol.*, 2014, 32, 760.
- 12 O. Yesil-Celiktas, S. Hassan, A. K. Miri, S. Mahajan, R. Al-kharboosh, A. Quiñones-Hinojosa and Y. S. Zhang, *Adv. Biosyst.*, 2018, 2, 1800109.
- 13 E. W. Esch, A. Bahinski and D. Huh, *Nat. Rev. Drug Discovery*, 2015, 14, 248.
- 14 K. Bhadriraju and C. S. Chen, *Drug Discovery Today*, 2002, 7, 612–620.
- 15 A. Polini, L. Prodanov, N. S. Bhise, V. Manoharan, M. R. Dokmeci and A. Khademhosseini, *Expert Opin. Drug Discovery*, 2014, 9, 335–352.
- 16 E. L. S. Fong, T. B. Toh, H. Yu and E. K.-H. Chow, *SLAS Technol.*, 2017, 22, 245–253.
- 17 D. W. Lee, S.-Y. Lee, L. Park, M.-S. Kang, M.-H. Kim, I. Doh, G. H. Ryu and D.-H. Nam, *SLAS Discovery*, 2017, 22, 645–651.
- 18 K. Bardsley, A. J. Deegan, A. El Haj and Y. Yang, in *Multi-Parametric Live Cell Microscopy of 3D Tissue Models*, Springer, 2017, pp. 3–18.
- 19 L. Teodori, A. Crupi, A. Costa, A. Diaspro, S. Melzer and A. Tarnok, *J. Biophotonics*, 2017, 10, 24–45.
- 20 T. Kilic, F. Navaee, F. Stradolini, P. Renaud and S. Carrara, *Microphysiol. Syst.*, 2018, 2, 5.
- 21 S. B. Kim, H. Bae, J. M. Cha, S. J. Moon, M. R. Dokmeci, D. M. Cropek and A. Khademhosseini, *Lab Chip*, 2011, 11, 1801–1807.
- 22 S. B. Kim, K.-i. Koo, H. Bae, M. R. Dokmeci, G. A. Hamilton, A. Bahinski, S. M. Kim, D. E. Ingber and A. Khademhosseini, *Lab Chip*, 2012, 12, 3976–3982.
- 23 Y. S. Zhang, J. Ribas, A. Nadhman, J. Aleman, Š. Selimović, S. C. Lesher-Perez, T. Wang, V. Manoharan, S. R. Shin, A. Damilano, N. Annabi, M. R. Dokmeci, S. Takayama and A. Khademhosseini, *Lab Chip*, 2015, 15, 3661–3669.
- 24 A. Feizi, Y. Zhang, A. Greenbaum, A. Guziak, M. Luong, R. Y. L. Chan, B. Berg, H. Ozkan, W. Luo, M. Wu, Y. Wu and A. Ozcan, *Lab Chip*, 2016, 16, 4350–4358.
- 25 S. K. J. Ludwig, H. Zhu, S. Phillips, A. Shiledar, S. Feng, D. Tseng, L. A. van Ginkel, M. W. F. Nielsen and A. Ozcan, *Anal. Bioanal. Chem.*, 2014, 406, 6857–6866.
- 26 H. Zhu, O. Yaglidere, T. W. Su, D. Tseng and A. Ozcan, Wide-field fluorescent microscopy on a cell-phone, *2011 Annual International Conference of the IEEE Engineering in Medicine and Biology Society*, 2011.
- 27 Y. S. Zhang, J.-B. Chang, M. M. Alvarez, G. Trujillo-de Santiago, J. Aleman, B. Batzaya, V. Krishnadoss, A. A. Ramanujam, M. Kazemzadeh-Narbat, F. Chen, P. W. Tillberg, M. R. Dokmeci, E. S. Boyden and A. Khademhosseini, *Sci. Rep.*, 2016, 6, 22691.
- 28 Y. S. Zhang, F. Busignani, J. Ribas, J. Aleman, T. N. Rodrigues, S. A. M. Shaegh, S. Massa, C. B. Rossi, I. Taurino, S.-R. Shin, G. Calzone, G. M. Amarasingha, D. L. Chambers, S. Jabari, Y. Niu, V. Manoharan, M. R. Dokmeci, S. Carrara, D. Demarchi and A. Khademhosseini, *Sci. Rep.*, 2016, 6, 22237.
- 29 T. Moons, L. V. Gool and M. Vergauwen, *Found. Trends. Comput. Graph. Vis.*, 2010, 4, 287–404.
- 30 P. M. Kulkarni, N. Rey-Villamizar, A. Merouane, N. Sudheendran, S. Wang, M. Garcia, I. V. Larina, B. Roysam and K. V. Larin, *Quant. Imaging Med. Surg.*, 2015, 5, 125–135.
- 31 J. Selb, A. M. Dale and D. A. Boas, *Opt. Express*, 2007, 15, 16400–16412.
- 32 B. W. Graf and S. A. Boppart, *Methods Mol. Biol.*, 2010, 591, 211–227.
- 33 A. Polat, N. Matela, A. Dinler, Y. S. Zhang and I. Yildirim, *Biomed. Signal Process. Control*, 2019, 48, 26–34.
- 34 Y. S. Zhang, F. Davoudi, P. Walch, A. Manbachi, X. Luo, V. Dell'Erba, A. K. Miri, H. Albadawi, A. Arneri, X. Li, X. Wang, M. R. Dokmeci, A. Khademhosseini and R. Oklu, *Lab Chip*, 2016, 16, 4097–4105.
- 35 K. Yue, G. Trujillo-de Santiago, M. M. Alvarez, A. Tamayol, N. Annabi and A. Khademhosseini, *Biomaterials*, 2015, 73, 254–271.
- 36 Y. Zhou, T. Arai, Y. Horiguchi, K. Ino, T. Matsue and H. Shiku, *Anal. Biochem.*, 2013, 439, 187–193.
- 37 T. Okuyama, H. Yamazoe, N. Mochizuki, A. Khademhosseini, H. Suzuki and J. Fukuda, *J. Biosci. Bioeng.*, 2010, 110, 572–576.
- 38 S. F. Wong, D. Y. No, Y. Y. Choi, D. S. Kim, B. G. Chung and S.-H. Lee, *Biomaterials*, 2011, 32, 8087–8096.
- 39 N. S. Bhise, V. Manoharan, S. Massa, A. Tamayol, M. Ghaderi, M. Miscuglio, Q. Lang, Y. S. Zhang, S. R. Shin, G. Calzone, N. Annabi, T. Shupe, C. Bishop, A. Atala, M. R. Dokmeci and A. Khademhosseini, *Biofabrication*, 2016, 8, 014101.
- 40 S. R. Shin, Y. S. Zhang, D. Kim, A. Manbohi, H. Avci, A. Silvestri, J. Aleman, N. Hu, T. Kilic, W. Keung, M. Righi, P. Assawes, H. A. Alhadrami, R. A. Li, M. R. Dokmeci and A. Khademhosseini, *Anal. Chem.*, 2016, 88, 10019–10027.
- 41 S. R. Shin, T. Kilic, Y. S. Zhang, H. Avci, N. Hu, D. Kim, C. Branco, J. Aleman, S. Massa, A. Silvestri, J. Kang, H. A. Hussaini, M. A. Hussaini, J. Lee, S.-K. Chae, H. Lee, M. R. Dokmeci and A. Khademhosseini, *Adv. Sci.*, 2017, 4(5), 1600522.

- 42 A. Skardal, S. V. Murphy, M. Devarasetty, I. Mead, H.-W. Kang, Y.-J. Seol, Y. S. Zhang, S.-R. Shin, L. Zhao, J. Aleman, A. Hall, T. Shupe, A. Kleensangb, M. R. Dokmeci, S. J. Lee, J. Jackson, J. Yoo, T. Hartung, A. Khademhosseini, S. Soker, C. Bishop and A. Atala, *Sci. Rep.*, 2017, **7**, 8837.
- 43 Y. S. Zhang, J. Aleman, S. R. Shin, T. Kilic, D. Kim, S. A. M. Shaegh, S. Massa, R. Riahi, S.-K. Chae, N. Hu, H. Avci, W. Zhang, A. Silvestri, A. Manbohi, A. Polini, G. Calzone, N. Shaikh, A. Sanati, P. Alerasool, N. S. Bhise, E. Budina, A. Pourmand, A. Skardal, T. Shupe, C. Bishop, M. R. Dokmeci, A. Atala and A. Khademhosseini, *Proc. Natl. Acad. Sci. U. S. A.*, 2017, **114**, E2293–E2302.
- 44 W. Liu, Y. S. Zhang, M. A. Heinrich, F. De Ferrari, H. L. Jang, S. M. Bakht, M. M. Alvarez, J. Yang, Y.-C. Li, G. Trujillo-de Santiago, A. K. Miri, K. Zhu, P. Khoshakhlagh, G. Prakash, H. Cheng, X. Guan, Z. Zhong, J. Ju, G. H. Zhu, X. Jin, S. R. Shin, M. R. Dokmeci and A. Khademhosseini, *Adv. Mater.*, 2017, **29**, 1604630.
- 45 K. Yue, X. Li, K. Schrobback, A. Sheikhi, N. Annabi, J. Leijten, W. Zhang, Y. S. Zhang, D. W. Hutmacher and T. J. Klein, *Biomaterials*, 2017, **139**, 163–171.
- 46 Y. S. Zhang, M. Duchamp, L. W. Ellisen, M. A. Moses and A. Khademhosseini, presented in part at the AACR 2017, Washington DC, 2017.
- 47 M. Beister, D. Kolditz and W. A. Kalender, *Phys. Med.*, 2012, **28**, 94–108.
- 48 J. Peterson, B. N. P. Paulsson and T. V. McEvilly, *Applications of algebraic reconstruction to crosshole seismic data*, 1985.
- 49 S. Kaczmarz, *Bull. Int. Acad. Pol. Sci. Lett., Cl. Med.*, 1937, **35**, 355–357.
- 50 G. T. Herman and L. B. Meyer, *IEEE Trans. Med. Imaging*, 1993, **12**, 600–609.
- 51 N. Chetih and Z. Messali, Tomographic image reconstruction using filtered back projection (FBP) and algebraic reconstruction technique (ART), 2015 *3rd International Conference on Control, Engineering & Information Technology (CEIT)*, 2015.
- 52 R. L. Siddon, *Fast calculation of the exact radiological path for a three-dimensional CT array*, 1985.
- 53 D. L. Donoho, *IEEE Trans. Inf. Theory*, 2006, **52**, 1289–1306.
- 54 L. I. Rudin, S. Osher and E. Fatemi, *Phys. D*, 1992, **60**, 259–268.
- 55 S. Fantini, M.-A. Franceschini, J. B. Fishkin and E. Gratton, *Proc. SPIE*, 1994, **2131**, 356–364.
- 56 S. Ravishankar and Y. Bresler, *IEEE Trans. Signal Process.*, 2013, **61**, 1072–1086.
- 57 P. Diemoz, A. Bravin, M. Langer and P. Coan, *Opt. Express*, 2012, **20**, 27670–27690.
- 58 M. Nomi, A. Atala, P. D. Coppi and S. Soker, *Mol. Aspects Med.*, 2002, **23**, 463–483.
- 59 R. K. Jain, P. Au, J. Tam, D. G. Duda and D. Fukumura, *Nat. Biotechnol.*, 2005, **23**, 821–823.
- 60 J. Rouwkema, N. C. Rivron and C. A. van Blitterswijk, *Trends Biotechnol.*, 2008, **26**, 434–441.
- 61 H. Bae, A. S. Puranik, R. Gauvin, F. Edalat, B. Carrillo-Conde, N. A. Peppas and A. Khademhosseini, *Sci. Transl. Med.*, 2012, **4**, 160ps123.
- 62 Y. S. Zhang, K. Yue, J. Aleman, K. Moghaddam, S. M. Bakht, V. Dell'Erba, P. Assawes, S. R. Shin, M. R. Dokmeci, R. Oklu and A. Khademhosseini, *Ann. Biomed. Eng.*, 2017, **45**, 148–163.
- 63 J. Malda, J. Visser, F. P. Melchels, T. Jüngst, W. E. Hennink, W. J. A. Dhert, J. Groll and D. W. Hutmacher, *Adv. Mater.*, 2013, **25**, 5011–5028.
- 64 S. V. Murphy and A. Atala, *Nat. Biotechnol.*, 2014, **32**, 773–785.
- 65 J. S. Miller, K. R. Stevens, M. T. Yang, B. M. Baker, D.-H. T. Nguyen, D. M. Cohen, E. Toro, A. A. Chen, P. A. Galie and X. Yu, *Nat. Mater.*, 2012, **11**, 768–774.
- 66 L. E. Bertassoni, M. Cecconi, V. Manoharan, M. Nikkhah, J. Hjortnaes, A. L. Cristina, G. Barabaschi, D. Demarchi, M. R. Dokmeci and Y. Yang, *Lab Chip*, 2014, **14**, 2202–2211.
- 67 D. B. Kolesky, R. L. Truby, A. S. Gladman, T. A. Busbee, K. A. Homan and J. A. Lewis, *Adv. Mater.*, 2014, **26**, 3124–3130.
- 68 V. K. Lee, D. Y. Kim, H. Ngo, Y. Lee, L. Seo, S.-S. Yoo, P. A. Vincent and G. Dai, *Biomaterials*, 2014, **35**, 8092–8102.
- 69 X. Heng, D. Erickson, L. R. Baugh, Z. Yaqoob, P. W. Sternberg, D. Psaltis and C. Yang, *Lab Chip*, 2006, **6**, 1274–1276.
- 70 S. A. Lee, R. Leitao, G. Zheng, S. Yang, A. Rodriguez and C. Yang, *PLoS One*, 2011, **6**, e26127.
- 71 W. Mueller-Klieser, *J. Cancer Res. Clin. Oncol.*, 1987, **113**, 101–122.
- 72 G. Hamilton, *Cancer Lett.*, 1998, **131**, 29–34.
- 73 S.-A. Lee, D. Y. No, E. Kang, J. Ju, D.-S. Kim and S.-H. Lee, *Lab Chip*, 2013, **13**, 3529–3537.
- 74 R. M. Tostoes, S. B. Leite, M. Serra, J. Jensen, P. Bjorquist, M. J. Carrondo, C. Brito and P. M. Alves, *Hepatology*, 2012, **55**, 1227–1236.
- 75 S. J. Fey and K. Wrzesinski, *Toxicol. Sci.*, 2012, **127**, 403–411.
- 76 M. Crespo, E. Vilar, S.-Y. Tsai, K. Chang, S. Amin, T. Srinivasan, T. Zhang, N. H. Pipalia, H. J. Chen, M. Witherspoon, M. Gordillo, J. Z. Xiang, F. R. Maxfield, S. Lipkin, T. Evans and S. Chen, *Nat. Med.*, 2017, **23**, 878.
- 77 S. F. Boj, C.-I. Hwang, L. A. Baker, I. I. C. Chio, D. D. Engle, V. Corbo, M. Jager, M. Ponz-Sarvise, H. Tiriac, M. S. Spector, A. Gracanin, T. Oni, K. H. Yu, R. van Boxtel, M. Huch, K. D. Rivera, J. P. Wilson, M. E. Feigin, D. Öhlund, A. Handly-Santana, C. M. Ardito-Abraham, M. Ludwig, E. Elyada, B. Alagesan, G. Biffi, G. N. Yordanov, B. Delcuze, B. Creighton, K. Wright, Y. Park, F. H. M. Morsink, I. Q. Molenaar, I. H. B. Rinkes, E. Cuppen, Y. Hao, Y. Jin, I. J. Nijman, C. Iacobuzio-Donahue, S. D. Leach, D. J. Pappin, M. Hammell, D. S. Klimstra, O. Basturk, R. H. Hruban, G. J. Offerhaus, R. G. J. Vries, H. Clevers and D. A. Tuveson, *Cell*, 2015, **160**, 324–338.
- 78 D. Gao, I. Vela, A. Sboner, P. J. Iaquinta, W. R. Karthaus, A. Gopalan, C. Dowling, J. N. Wanjala, E. A. Undvall, V. K. Arora, J. Wongvipat, M. Kossai, S. Ramazanoglu, L. P.

- Barboza, W. Di, Z. Cao, Q. F. Zhang, I. Sirota, L. Ran, T. Y. MacDonald, H. Beltran, J.-M. Mosquera, K. A. Touijer, P. T. Scardino, V. P. Laudone, K. R. Curtis, D. E. Rathkopf, M. J. Morris, D. C. Danila, S. F. Slovin, S. B. Solomon, J. A. Eastham, P. Chi, B. Carver, M. A. Rubin, H. I. Scher, H. Clevers, C. L. Sawyers and Y. Chen, *Cell*, 2014, **159**, 176–187.
- 79 L. Broutier, G. Mastrogiovanni, M. M. A. Verstegeen, H. E. Francies, L. M. Gavarró, C. R. Bradshaw, G. E. Allen, R. Arnes-Benito, O. Sidorova, M. P. Gasparsz, N. Georgakopoulos, B.-K. Koo, S. Dietmann, S. E. Davies, R. K. Praseedom, R. Lieshout, J. N. M. Ijzermans, S. J. Wigmore, K. Saeb-Parsy, M. J. Garnett, L. J. W. van der Laan and M. Huch, *Nat. Med.*, 2017, **23**, 1424.
- 80 D. Tseng, O. Mudanyali, C. Oztoprak, S. O. Isikman, I. Senean, O. Yaglidere and A. Ozcan, *Lab Chip*, 2010, **10**, 1787–1792.
- 81 J. Garcia-Sucerquia, W. Xu, M. H. Jericho and H. J. Kreuzer, *Opt. Lett.*, 2006, **31**, 1211–1213.
- 82 F. Zhang, G. Pedrini and W. Osten, *Phys. Rev. A: At., Mol., Opt. Phys.*, 2007, **75**, 043805.
- 83 J. R. Fienup and C. C. Wackerman, *J. Opt. Soc. Am.*, 1986, **3**, 1897–1907.
- 84 J. Wu, G. Zheng and L. M. Lee, *Lab Chip*, 2012, **12**, 3566–3575.
- 85 D. Shin, M. Daneshpanah, A. Anand and B. Javidi, *Opt. Lett.*, 2010, **35**, 4066–4068.
- 86 Y. S. Zhang, M. Duchamp, R. Oklu, L. W. Ellisen, R. Langer and A. Khademhosseini, *ACS Biomater. Sci. Eng.*, 2016, **2**, 1710–1721.
- 87 Y. Adiguzel and H. Kulah, *Sensors*, 2012, **12**, 10042–10066.
- 88 S. Tabata, S. Yoshida, Y. Morimoto and S. Takeuchi, Catch a cell on a CMOS: Selective retrieval of single cell using a microplate technology performed on a CMOS imaging sensor, *2016 IEEE 29th International Conference on Micro Electro Mechanical Systems (MEMS)*, 2016.
- 89 T. Tokuda, T. Noda, K. Sasagawa and J. Ohta, *Materials*, 2010, **4**, 84–102.